ACS APPLIED NANO MATERIALS

Article

Cite This: ACS Appl. Nano Mater. 2020, 3, 274−282

www.acsanm.org

Surface-Induced Enhanced Band Gap in the (0001) Surface of Bi_2Se_3 Nanocrystals: Impacts on the Topological Effect

Soumendra Kumar Das and Prahallad Padhan*

Department of Physics, Indian Institute of Technology (IIT) Madras, Chennai 600036, India

ABSTRACT: The (0001)-oriented hexagon-shaped nanocrystal plates of Bi_2Se_3 are synthesized by the hot-injection method using a nontoxic solvent. The Bi_2Se_3 hexagonal plates have a thickness of around 40 nm with a lateral dimension of 600 nm. The selected-area high-resolution transmission electron microscopy images show hexagonal lattice fringes with a lattice spacing of the (0001)-oriented hexagonal crystal structure. These nanocrystals exhibit a band transition energy of ∼0.66 eV, which is 3 times that of Bi_2Se_3 single crystals. The first-principles density functional theory (DFT) calculations demonstrate that the expanded band gap (E_g) of these Bi_2Se_3 nanocrystals is due to the phenomenal surface band dispersion and the competition between covalent and van der Waals interactions that determines the topological state. The DFT calculations provide evidence for expansion of the (0001) surface E_g of Bi_2Se_3 from 0.3 to 0.63 eV with an increase of the surface for the same thickness. These Bi_2Se_3 nanocrystals dispersed between the Ag contact pads exhibit thermally activated behavior with Poole−Frenkel-type conduction due to the electron trapping/detrapping barriers between the nanocrystals. These results will further advance the understanding of fundamental charge-transport mechanisms in Bi_2Se_3, which can also be an essential parameter in the development of various electronic applications such as resistive memory switching and sensing devices.

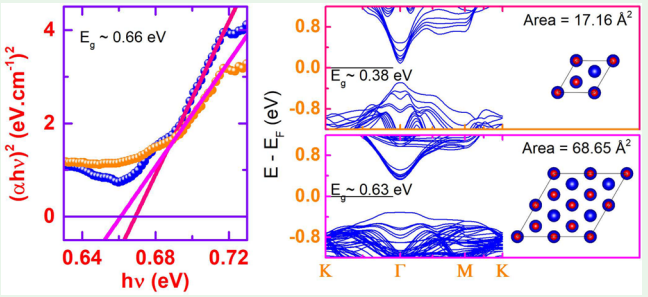

KEYWORDS: *topological insulator, Bi_2Se_3 nanocrystal, hot-injection method, density functional theory, band structure*

1. INTRODUCTION

Topological insulators (TIs) represent a new state of quantum materials that behave as insulators in bulk but possess metallic surface states on the edges or surfaces. These surface states are protected by time-reversal symmetry and become insensitive to backscattering by nonmagnetic impurities.[1] Among the various compounds showing TI properties, Bi_2Se_3 is of particular interest because of its simple layered structure, relatively larger band gap (E_g) of ∼0.3 eV, which is more compared to that of the room temperature energy scale, single Dirac cone at the Γ point, etc.[2] However, in reality, the surface effects of most of the TI materials get suppressed because of high carrier density and antisite defects.[3] Under these circumstances, the nanostructured synthesis of TIs has become an effective tool for enhancing the contribution of surface states toward the electrical transport and optical properties because they have a large surface-to-volume ratio. The physical properties of the nanostructures are entirely different compared to those of the bulk counterparts when the size is reduced to the nanoscopic range.[4]

A variety of nanodimensional morphologies, like spherical,[5] hexagonal-flake,[6] rectangular nanosheet,[7] triangular or hexagonal plate,[8,9] rod,[10] and ribbon,[11] of the Bi_2Se_3 have been synthesized using different techniques. Bi_2Se_3 nanocrystals with some of these morphologies are prepared by adopting a bottom-up approach, such as hydrothermal,[7] solvothermal,[10] polyol,[9] vapor−liquid−solid,[11] catalyst-free vapor−solid,[8] sonochemical,[12] and hot-injection[13] methods. In addition, nanodimensional Bi_2Se_3 crystals are also prepared using the top-down approach such as liquid-phase exfoliation,[14] electrochemical exfoliation,[15] and exfoliation by an atomic force microscopy tip.[16] Potential applications of Bi_2Se_3 for a wide range of devices working at room temperature require a large bulk E_g. Several techniques have been used to measure E_g of Bi_2Se_3. The reported range of E_g of Bi_2Se_3 single crystals is between 0.22 and 0.33 eV,[17,18] and that of the thin films varies between 0.1 and 2.0 eV.[19−21] The disparity of E_g of Bi_2Se_3 is widely explained by its thickness dependence.[6,22] The direct E_g (0.332 ± 0.055 eV) type of Bi_2Se_3 single crystals is evident from angle-resolved photoemission spectroscopy (ARPES) through a 3D band mapping in a large fraction of the Brillouin zone.[18] A relatively lower value of E_g (0.22 eV) has been established for the single crystal Bi_2Se_3 from the combined magnetotransport, photoluminescence, and IR transmission experiments.[17] E_g of the Bi_2Se_3 thin films has been found to be 0.1 eV, which was explained by the possibility of the in-gap impurity states.[19] The finite density of in-gap states has been confirmed from the differential conductance spectra of an atomically resolved Bi_2Se_3 surface.[23] The actual excitation energy could be different because of the presence of Pauli

Received: October 7, 2019
Accepted: December 11, 2019
Published: December 11, 2019

DOI: 10.1021/acsanm.9b01941
ACS Appl. Nano Mater. 2020, 3, 274−282

blocking of the states below E_F in the conduction band; thus, the Burstein–Moss effect correction is important, which increases E_g.[24] The nanodimensional Bi_2Se_3 single crystals are expected to be surface-dominated. The reported values of E_g of the nanodimensional Bi_2Se_3 vary between 0.6 and 2.6 eV.[6,25] Most of the reports have used absorption spectroscopy but did not measure the absorption spectra in the proper energy range and observed larger E_g; for example, the nanoflakes of 2–6 quintuple layer (QL) Bi_2Se_3 with an average lateral size of ∼7 nm have shown a larger band gap of 2 eV < E_g < 2.6 eV, which is explained by 0D confinement.[6] The rodlike Bi_2Se_3 nanostructures with an average diameter of 50 nm and an average length of 4 μm show optical E_g ∼ 1.5 eV, and the larger E_g value is usually explained by the quantum size effect.[10] However, in some reports, the absorption spectrum was measured up to ∼0.4 eV, but still E_g of the nanodimensional Bi_2Se_3 is larger than 0.3 eV. For example, the 1.4–2-nm-thick nanoflakes show E_g ∼ 0.6 eV,[25] while the hexagonal plates exhibit E_g ∼ 0.85 eV.[13]

The surface structure and states of Bi_2Se_3 govern the stability of the topological properties. Any alteration of the surface structure such as the diffusion, segregation, partial or complete oxidation, and vacancies at the surface changes the conductance of the topologically protected surface states. The surface states and related surface structure of (0001)-oriented Bi_2Se_3 have been extensively studied by X-ray photoelectron spectroscopy (XPS), including angle-resolved XPS (ARXPS) for the surface elemental composition, chemical state, and surface oxidation.[26] In the as-grown nanoribbons, a BiO_x peak is observed in the Bi 4f core-level spectra, and the intensity keeps growing as the exposure time to air increases along with an increase in the thickness of BiO_x. In contrast, for the Se 3d core-level spectra, a SeO_x layer whose intensity is very low for the as-grown sample is also formed and gradually increases with an increase of air-exposure time.[26] The exfoliated (0001)-oriented Bi_2Se_3 exposed to ambient air exhibits a broad peak at ∼59 eV near Se 3d and a shoulder toward the higher binding energy side of the Bi 5d regions, confirming oxidation of both Bi and Se at the surface.[27] In Bi 4f–Se 3p core-level spectra, the shifting of Se-related peaks (2.5 eV) toward the lower binding energy and Bi-related peaks (0.7 eV) toward the higher binding energy with respect to pure elemental aggregates shows a net charge flow with hybridized bonds between Bi and Se.[28]

The natural Se vacancies in the as-grown crystals of Bi_2Se_3 perform electron doping. Thus, the transport properties of Bi_2Se_3 are generally dominated by bulk conduction. In particular, the temperature dependence of the electrical resistivity is metallic-like,[4,29] and Shubnikov–de Haas (SdH) oscillations in the longitudinal resistivity show the characteristic signatures for a 3D Fermi surface.[29] The nanoplates and nanobeams of Bi_2Se_3 exhibit SdH oscillations, which suggest the presence of π Berry's phase and confirm the quantum transport of surface Dirac Fermions.[30] The nanoribbons of Bi_2Se_3 show Aharonov–Bohm oscillations in the magnetoresistance measurements due to the periodic quantum interference effects. The dominance of h/e oscillations (h is Planck's constant and e is the electron charge) and its temperature dependence show the robustness of the surface states.[11] The high field in the Hall resistance and low-field magnetoresistance measurements open up the possibility that topological surface states may coexist with a layered 2D electron system. Quantum oscillations in the Hall resistance, observed at temperatures of up to 50 K along with a high electron density (2×10^{19} cm^{-3}), and angular and temperature-dependent Hall resistance help to identify the 3D and 2D contributions to the transport behavior.[31] Transport measurement for a single nanoplate at low temperature with a high-k dielectric top gate shows a decrease in the carrier concentration with a highly tunable chemical potential with a weak antilocalization effect.[8] The 25-nm-diameter nanoparticles of Bi_2Se_3 synthesized using a sonochemical method exhibit 0.28% efficiency as a photocatalyst for the decolorization of rhodamine B and methylene blue using UV radiation.[12] The rectangular nanosheets of Bi_2Se_3 synthesized using a thermochemical method show a superior performance with a large discharge capacity of ∼725.6 mAh g^{-1} compared to the spherical nanosheets prepared using hydrothermal techniques, with a reduced value of ∼419.6 mAh g^{-1}.[7] Hexagonal flakes like Bi_2Se_3 prepared by a solvothermal method exhibit thermoelectric properties with a figure of merit of 0.096 at 523 K.[32]

First-principles density functional theory (DFT) calculations have been performed with spin–orbit coupling (SOC) effects to study various properties of Bi_2Se_3. The DFT calculations show several interesting unique features of Bi_2Se_3; for example, the study of phonon dispersion in Bi_2Se_3 shows that the frequencies of the soft modes of two acoustic branches along the Z–F and Γ–F directions are imaginary and oscillating in nature.[33] Studies of the electronic structure indicate that the properties of Bi_2Se_3 are controlled by the p orbitals rather than the s orbitals.[34] E_g of a single QL of Bi_2Se_3 is 0.41 eV, which decreases to 0.23 eV with an increase of the number of QLs from 1 to 6.[35] A single QL of Bi_2Se_3 shows a larger thermoelectric figure of merit (0.27) compared to the bulk value (0.10), which further increases to 0.30 with 2.5% compressive strain.[35] The incorporation of a van der Waals density functional with Cooper's exchange in first-principles electronic structure calculations correctly predicts the experimental interlayer distances in unstrained Bi_2Se_3 and Bi_2Te_3. The calculations also show that the E_g decreases for tensile strain and increases for compressive stress. Using the semiclassical Boltzmann approach, it is predicted that the Seebeck coefficient of Bi_2Te_3 increases for in-plane compressive strain, while that of Bi_2Se_3 increases for in-plane tensile strain. In addition, the in-plane power factor of n-doped Bi_2Se_3 increases for compressive uniaxial strain, while that of Bi_2Te_3 increases for compressive biaxial strain.[36]

Different techniques for the synthesis of a nanostructure have been developed that involve the use of highly expensive and toxic solvents like trioctylphosphine, 1-dodecanethiol, etc.[37] In this paper, we report a simple way to synthesize Bi_2Se_3 nanostructures by the hot-injection method using nontoxic solvents. The (0001)-oriented hexagonal-shaped platelike morphology of Bi_2Se_3 is confirmed from transmission electron microscopy (TEM), while the hexagonal crystal structure of these nanocrystals is established by X-ray diffraction (XRD). E_g of these hexagonal plates is 0.66 eV, nearly 3 times that of the Bi_2Se_3 single crystals. Using the first-principles DFT calculations, we demonstrate that the larger E_g of these hexagonal nanocrystals could be due to the surface effect.

2. RESULTS AND DISCUSSION

The Bi_2Se_3 crystallizes in a hexagonal structure with space group $R\bar{3}m$ (D_{3d}^5). The conventional unit cell contains 15 atoms. Bi_2Se_3 has a layered structure with five atomic layers

DOI: 10.1021/acsanm.9b01941
ACS Appl. Nano Mater. 2020, 3, 274–282

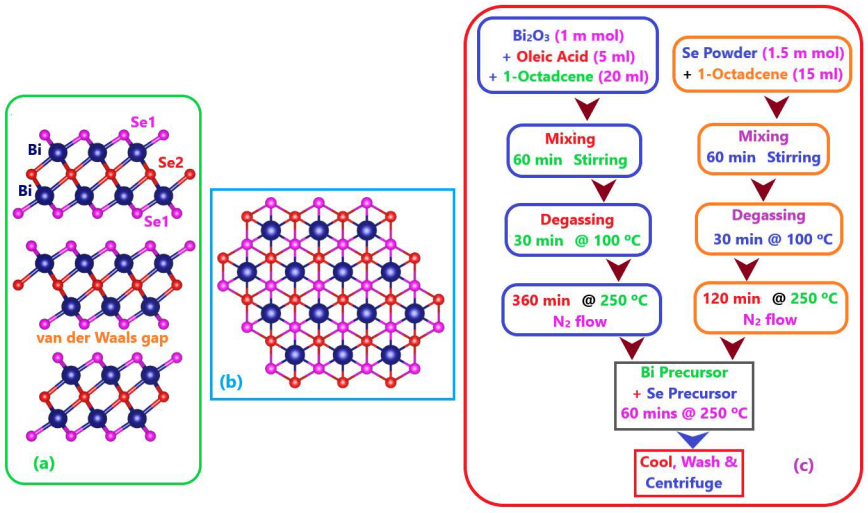

Figure 1. (a) Unit cell of the $(10\bar{1}0)$ surface of Bi_2Se_3 consisting of three QLs. Each QL consists of five atomic layers in the order Se1−Bi−Se2−Bi−Se1. The QLs are bound by the weak van der Waals force. (b) (0001) surface of Bi_2Se_3 with Se1−Bi−Se2 layers. (c) Reaction pathway for the preparation of Bi_2Se_3 nanocrystals in the hot-injection method.

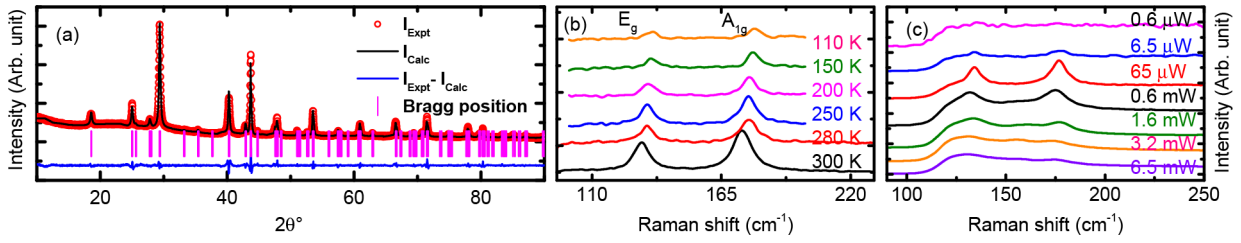

Figure 2. (a) $\theta-2\theta$ XRD pattern and Rietveld refinement profile and (b−c) Raman spectra of the Bi_2Se_3 hexagonal plates synthesized at 250 °C. The Raman spectra were measured at different temperatures with 10 mW excitation laser (b) and room temperature with different optical densities (c).

arranged in a particular order called QL along the z direction. There are three QLs (Figure 1a) in a conventional hexagonal unit cell. Each QL consists of five atomic layers in the order Se1−Bi−Se2−Bi−Se1 (Figure 1a). Within a QL, the interaction is a strongly covalent, whereas inter-QL interaction is of a weak van der Waals type. The thickness of each QL is about 0.96 nm.[38] The Se2 layer acts as the inversion center and is different from the Se1 layer. There are three crystallographic axes in the unit cell. It has a trigonal axis with 3-fold rotation symmetry (defined as the z axis), a binary axis with 2-fold rotation symmetry (defined as the x axis), and a bisectrix axis in the reflection plane (defined as the y axis). Because of the presence of inversion symmetry, the topological invariant can be calculated through the parity of occupied bands at the Γ point.[2] Figure 1b shows the (0001)-oriented surface of Bi_2Se_3 with the top three layers of a QL.

Hexagonal-shaped nanocrystals of Bi_2Se_3 were prepared by adopting a chemical hot-injection method with a mechanical and magnetic stirring mechanism (Figure 1c). The nucleation and growth of (0001)-oriented hexagonal-shaped nanocrystals could be due to the anisotropic bonding existing near the weak van der Waals interaction between the QLs[8,39] and/or the supersaturation level of the reaction system, which represents the driving force for crystal growth.[40] The $\theta-2\theta$ XRD patterns of the Bi_2Se_3 nanocrystals resemble the characteristic peaks of the hexagonal structure irrespective of the stirring mechanism. Figure 2a shows a typical XRD pattern of the Bi_2Se_3 nanocrystals synthesized at 250 °C. This XRD pattern does not show any peak due to the parasitic or impurity phases. Figure 2a also includes the curve simulated using the Rietveld refinement technique. The crystal structures of these nanocrystals are established from the Rietveld refinement analysis, which confirms the $R\bar{3}m$ (D_{3d}^5) crystallographic group of Bi_2Se_3. Refinement of the XRD spectrum with a high degree of precision reveals the cell parameters a = 4.136 Å and c = 28.59 Å. However, variation of the different synthesis temperatures changes the a value from −0.08% to −0.17% and the c value from −0.06% to −0.43%. The crystal structure observed in Figure 2a was further confirmed by the Raman spectra of these nanocrystals in the assessable Raman shift range (Figure 2b) of the Raman spectrometer. At room temperature the Raman line appearing at ∼131.2 cm^{-1} corresponds to the E_g mode due to the in-plane vibrations of the Se and Bi atoms, while the other peak at ∼173.4 cm^{-1} corresponds to the A_{1g} mode, which reflects the out-of-plane vibrations of the Se and Bi atoms.[9] Thus, the A_{1g} mode is more sensitive to the thickness of the nanocrystal and interlayer van der Waals interactions, which influence the effective restoring forces acting on these atoms.[9] The Raman spectra of these Bi_2Se_3 nanocrystals were recorded at various temperatures. As these Bi_2Se_3 nanocrystals are cooled to 110 K, the E_g and A_{1g} modes show blue shifts of up to 5 and 6 cm^{-1}, respectively (Figure 2b), and this can be due to thermal contraction, which usually results in anharmonicity.[41,42] In addition, the full width at half-maximum of these peaks decreases with a decrease in the temperature, which indicates an increase in the phonon lifetime or relaxation time.

DOI: 10.1021/acsanm.9b01941
ACS Appl. Nano Mater. 2020, 3, 274−282

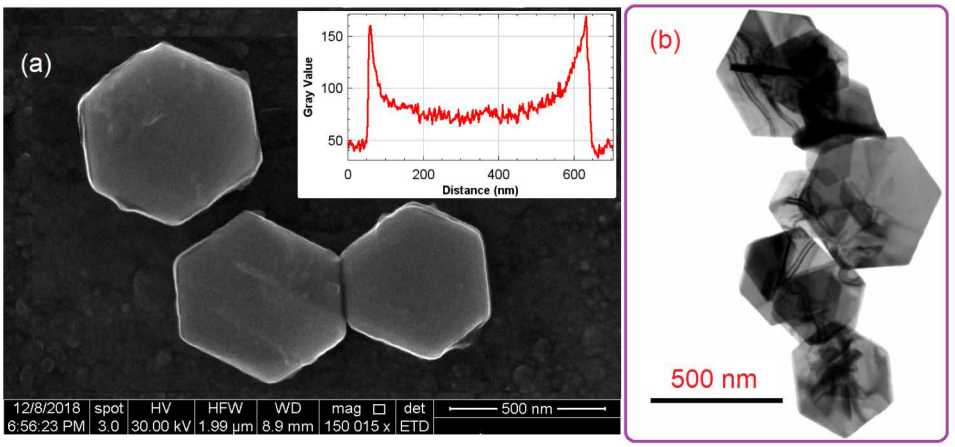

Figure 3. (a) High-magnification FESEM and (b) low-magnification TEM images of the Bi_2Se_3 hexagonal plates synthesized at 250 °C. The inset of part a shows a plot profile of the top hexagonal plate.

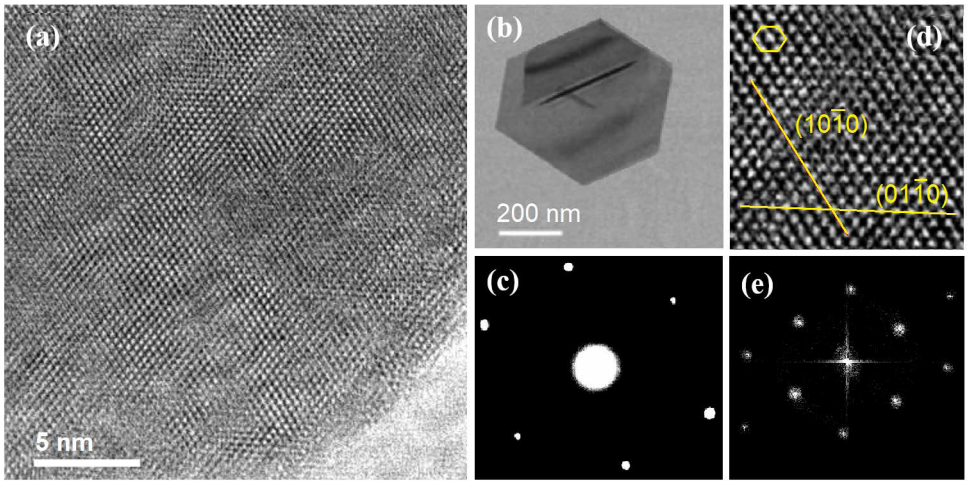

Figure 4. (a) HRTEM image, (b) a single hexagonal plate with a flat surface and sharp edges, (c) SAED pattern, (d) a section of the zoomed HRTEM image, and (e) fast Fourier transform of the HRTEM image of the Bi_2Se_3 nanocrystals synthesized at 250 °C.

The anharmonicity present in the crystal could lead to a change in the vibrational energy of the optical phonon mode, which results in a decay of the optical mode either into two acoustic modes of equal and opposite momentum (Klemens channel) or one optical and one acoustic phonon (Ridley channel).[41] At room temperature, the Raman spectra of the Bi_2Se_3 nanocrystals are strongly influenced by the excitation optical density. At 0.65 μW excitation laser power, the Raman modes of Bi_2Se_3 are not observed, but as the laser power is increased to 6.5 μW, the E_g^2 and A_{1g}^2 modes start to appear in the Raman spectra of the Bi_2Se_3 nanocrystals (Figure 2c). The E_g^2 and A_{1g}^2 modes in the Raman spectra of the Bi_2Se_3 nanocrystals are distinct and sharp at 65 μW laser power. When the laser power is further increased, these Raman peaks become broad and shift toward lower frequency because of the excitation-induced laser heating effect.[9]

The field-emission scanning electron microscopy (FESEM) images of Bi_2Se_3 prepared at different temperatures (Figure 3a) reveal that the as-synthesized Bi_2Se_3 nanocrystals have regular as well as truncated shape and size with hexagonal plate morphology. The inset shows the plot profile of a hexagonal plate, which indicates that the lateral dimension of the plate is around 600 nm. The hexagonal plate morphology was further confirmed from the bright-field TEM images (Figure 3b).

The high-resolution TEM (HRTEM) images of these hexagonal plates of Bi_2Se_3 (Figure 4a) show lattice fringes with hexagonal crystal structure, consistent with those of Figure 3a. A typical hexagonal plate of Bi_2Se_3 synthesized at 250 °C for 1 h has a flat surface and sharp edges (Figure 4b). This Bi_2Se_3 hexagonal plate has a thickness of around 40 nm with a lateral dimension of 600 nm, which is consistent with that of the SEM image. The selected-area electron diffraction (SAED) patterns show a 2-fold-symmetry reciprocal-space diffraction spot pattern (Figure 4c) and indicate the single-crystalline nature of the Bi_2Se_3 hexagonal plate. The SAED pattern can be indexed as a 2-fold symmetry along the zone axis [0001], which demonstrates that the nanocrystal grows along [0001], with the (0001) facet as top and bottom surfaces with a minimal distortion along [01$\bar{1}$0] of the (01$\bar{1}$0) facet and a significant distortion along [10$\bar{1}$0] of the (10$\bar{1}$0) facet. A selected-area zoomed HRTEM image (Figure 4d) shows hexagonal lattice fringes with a lattice spacing of $d_{10\bar{1}0} \sim 3.462$ Å and $d_{01\bar{1}0} \sim 4.022$ Å, corresponding to the (10$\bar{1}$0) and (01$\bar{1}$0) planes, respectively. Further, the d spacing observed in the fast Fourier transform of the HRTEM image (Figure 4e) is consistent with the lattice spacing and SAED pattern.

XPS of these Bi_2Se_3 nanocrystals was performed to elucidate the surface chemical states and composition. Figure 5a shows

DOI: 10.1021/acsanm.9b01941
ACS Appl. Nano Mater. 2020, 3, 274−282

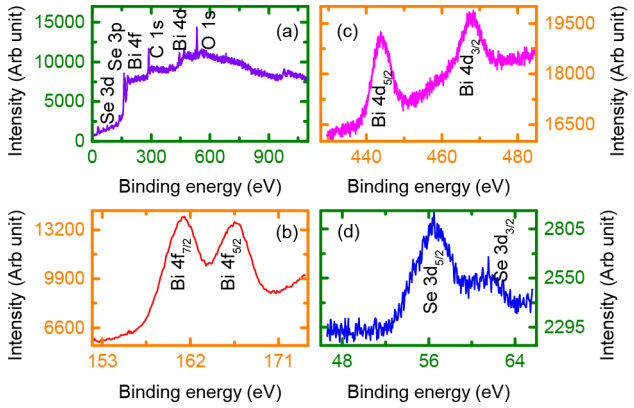

Figure 5. (a) Wide-scan and core-level XPS spectra of (b) Bi 4f, (c) Bi 4d, and (d) Se 3d of the Bi_2Se_3 nanocrystals synthesized at 250 °C.

the low-resolution XPS spectrum, indicating the presence of Bi, Se, C, and O species. The presence of C- and O-related adsorbed species is likely due to the surface hydrocarbon contaminants and moisture uptake.[43] The high-resolution spectrum of Se 3d in the Bi_2Se_3 nanocrystal shows a broad peak and can be fitted with an energy of 56.26 eV (Figure 5d), which lies between Se $3d_{5/2}$ and $3d_{3/2}$ compared to pure bulk Se,[44] while the high-resolution spectrum of Bi 4f in the Bi_2Se_3 nanocrystal can be fitted perfectly using the two peaks for Bi $4f_{7/2}$ and $4f_{5/2}$ at 161.0 and 166.38 eV, respectively, separated by 5.38 eV (Figure 5b). The observed spin−orbital splitting of Bi $4f_{7/2}$ and $4f_{5/2}$ in the Bi_2Se_3 nanocrystal is very close to that of pure bulk Bi 4f. The high-resolution spectra of Bi 4d in the Bi_2Se_3 nanocrystal can be successfully fitted using the two peaks for Bi $4d_{5/2}$ and $4d_{3/2}$ at 443.58 and 466.60 eV, respectively (Figure 5c). The Bi $4d_{5/2}$ and $4d_{3/2}$ peaks show blue shifts of about 4.0 and 3.58 eV compared to that of pure bulk.[44] The more electronegative Se (2.55 in the Pauling scale) pulls a greater portion of the electron cloud toward itself compared to the less electronegative Bi (2.02 in the Pauling scale), thus pertaining to some ionic nature of the bonds in the Bi_2Se_3 crystal.[45] The absence of BiO or SeO peaks in the XPS spectra indicates that the surface structure and states of these nanocrystals are stable even after exposure to the atmosphere.[26]

The dispersed hexagonal Bi_2Se_3 nanocrystals, from the transmission measurement showing the behavior of the absorption coefficient up to an energy of 0.73 eV, is plotted in Figure 6a. The Tauc plot shows the lowest direct band transition around 0.66 eV, which is larger than the values for the Bi_2Se_3 single crystal.[17] The effect of the capping agent on the absorption spectra was studied by recording the absorption spectra of $CoFe_2O_4$ nanocrystals synthesized using 1-octadecne and oleic acid. The absorption spectra of the nanocrystal of $CoFe_2O_4$ do not reproduce the absorption spectra of Bi_2Se_3 in the energy range of 0.5−0.8 eV, which confirmed that the observed energy gap of the Bi_2Se_3 nanocrystal is not due to the capping agent. However, the observed E_g is nearly the same as the reported experimental values for the Bi_2Se_3 thin films,[46,47] the nanoplates, and the nanoflake.[13,25] The E_g of Bi_2Se_3 usually varies with the synthesis techniques,[6,10,14,17] morphology,[48,49] thickness,[6,19,22] and surface properties,[48,49] which account for quantum confinement along the different directions and surface energy states that could trap charge carriers at the surface.[6,14] A similar study of the quantum confinement effect was reported for the exfoliated Bi_2S_3 nanoribbons, which show larger E_g values compared to the bulk.[50] For hexagonal-shaped Bi_2Se_3 nanocrystals, probably due to the atomic configuration along [0001], the quantum confinements might be stronger along [0001] because the length is smaller than that in the other directions.

The band structure of the Bi_2Se_3 slabs were investigated using first-principles DFT calculations both without and with SOC effects using the *Quantum Espresso* (QE) code.[51] The in-plane lattice parameters were fixed to their experimental value (4.136 Å). The bulk band structure calculations were carried out after relaxing the atomic coordinates of the Bi_2Se_3 unit cell. Without SOC, the band structure of the bulk Bi_2Se_3 shows direct band gap with $E_g \approx 0.38$ eV, which is very closed to the reported experimental values.[17,18] The simulated E_g is smaller than E_g of the nanocrystals; thus, the bulk Bi_2Se_3 contribution is negligible. The incorporation of SOC changes in the direct band gap to an indirect band gap with $E_g \approx 0.19$ eV as the valence band maximum (VBM) and conduction band minimum (CBM) move away from the Fermi energy (E_F). The surface-to-volume ratio of the hexagonal Bi_2Se_3 nanocrystal is expected to be larger; thus, the influence of the surface states can control the direct band transition. The consequences of variation of the surface-to-volume ratio on the band structure of the Bi_2Se_3 slabs were studied after the atomic coordinates were relaxed to their minimum-energy values with 15 Å vacuum on the top QL in each case. The E_g value of the (0001) surface of the single QL Bi_2Se_3 is 0.97 eV, which is exceptionally higher than the bulk value of 0.22 eV (Figure 6f).[17] As the number of QLs increases to two, the E_g value of

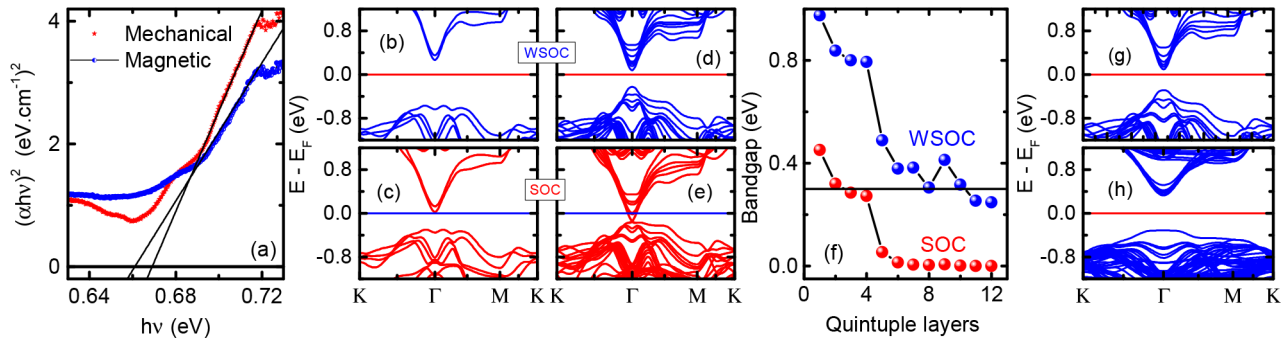

Figure 6. (a) Tauc plot of the Bi_2Se_3 nanocrystals synthesized at 250 °C using a mechanical and magnetic stirrer. The (0001) surface band structure without and with SOC of two- (b and c) and eight- (d and e) QLs-thick Bi_2Se_3, respectively. (f) Thickness-dependent (0001) surface band gap without and with SOC of Bi_2Se_3. The (0001) surface band structure of the six-QLs-thick Bi_2Se_3 with (g) 30 atoms and (h) 120 atoms.

DOI: 10.1021/acsanm.9b01941
ACS Appl. Nano Mater. 2020, 3, 274−282

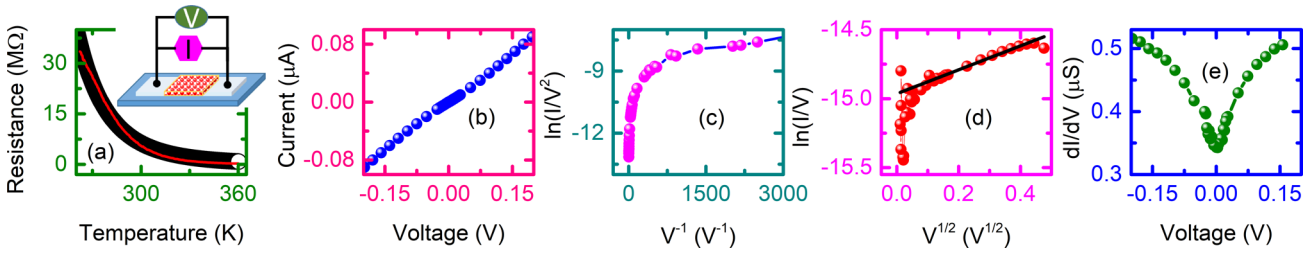

Figure 7. (a) Temperature-dependent resistance, (b) voltage-dependent current, (c) Fowler–Nordheim (F–N) plot, (d) Poole–Frenkel plot, and (e) differential conductance plot of the Bi_2Se_3 nanocrystals synthesized at 250 °C. The inset in part a shows the schematic of the experimental configuration for the transport measurement.

the (0001) surface of Bi_2Se_3 decreases to 0.83 eV, and the corresponding band structure (Figure 6b) shows an indirect E_g, with the CBM associated with the p_z orbital of the Bi atoms appearing at the Γ point. However, the VBM is deformed to M shape at the Γ point because of dispersion of the p orbitals of the Se atoms along the Γ–M and Γ–K directions. For three QLs, the E_g value of the (0001) surface of the Bi_2Se_3 further decreases to 0.79 eV because of a decrease in the van der Waals gap after relaxation. An indirect E_g is observed for the (0001) surface of Bi_2Se_3 with a thickness up to five QLs. A similar thickness-dependent E_g study has been performed by another group.[35] However, our E_g calculations show comparatively larger values for each QL. In addition, reports on the thickness-dependent WSOC E_g variation of Bi_2Se_3 are very scarce. In contrast, for six QL, E_g of the (0001) surface of Bi_2Se_3 is direct with a reduced magnitude of 0.379 eV. As the number of QLs increases, E_g of the (0001) surface of Bi_2Se_3 gradually decreases up to six QLs and then becomes saturated at around 0.3 eV for higher QLs (Figure 6f). In addition, the p_z orbitals of the Bi and Se atoms move toward E_F (Figure 6d). The shape of the p orbitals of the Se atoms of the (0001) surface of Bi_2Se_3 also becomes narrow with an increase in QLs, which was relatively flat for lower QLs. E_g of the (0001) surface of Bi_2Se_3 was reduced with the incorporation of SOC for the entire range of QLs. For example, E_g of the (0001) surface of Bi_2Se_3 of two QLs reduces from 0.837 to 0.32 eV with SOC (Figure 6b,c). As the number of QL increases from one, E_g of the (0001) surface of Bi_2Se_3 decreases and becomes zero for a thickness larger than six QLs (Figure 6f) with the formation of a single Dirac cone at the Γ point (Figure 6e), which indicates the appearance of the topological phase. Our result suggests that E_g of the (0001) surface of Bi_2Se_3 strongly depends on the number of QLs. For one QL, Bi_2Se_3 has only covalent interactions, but van der Waals interactions appear for Bi_2Se_3 with two QLs, and the competition between the two interaction processes starts with an increase of the QLs. Thus, the (0001) surface of Bi_2Se_3 is a normal insulator if the surface is dominating over the volume or the covalent interaction suppresses the van der Waals interaction.

Further, E_g of the (0001) surface of Bi_2Se_3 was calculated by increasing the surface area of the six-QL slab. In this structural configuration, the thickness of the six-QL slab remains the same, but the surface area is increased by 4 times; thus, the surface-to-volume ratio is unchanged. Surprisingly, E_g of the (0001) surface of Bi_2Se_3 is increased to 0.63 eV even though the surface-to-volume ratio is the same (Figure 6g,h). The expansion of E_g of the (0001) surface of Bi_2Se_3 with an increase of the surface area for the same thickness is attributed to enhancement of the covalent interaction compared to the van der Waals interaction. E_g of the (0001) surface of Bi_2Se_3 calculated using DFT is close to that of the hexagonal-shaped nanocrystal, which suggests that band dispersion due to the surface contribution in the nanocrystal dominately controls E_g. Thus, E_g of the hexagonal-shaped Bi_2Se_3 nanocrystal is expanded compared to that of its bulk because of the larger lateral size (600 nm) compared to the thickness (40 nm); i.e., band dispersion of the surface prevails. The hexagonal-shaped Bi_2Se_3 are dispersed between the two electrodes to measure the resistance. The resistance of the Bi_2Se_3 nanocrystals is 232 kΩ at 360 K. When these nanocrystals are cooled below 360 K, the resistance increases monotonically and becomes 33.2 MΩ at ∼260 K (Figure 7a). The solid line is the fit to the data for the expression $R \propto e^{-E_a/k_BT}$, which confirms that conduction of the Bi_2Se_3 nanocrystals is thermally activated.[52] The room temperature current–voltage characteristic of these Bi_2Se_3 nanocrystals shows nonlinear conduction, a deviation from the linearity around ±30 nA, i.e., in the vicinity of the Dirac cone (Figure 7b). At room temperature, the thermally activated electrons injected from one Bi_2Se_3 nanocrystal to another over the barrier result from electron trapping/detrapping. In addition, the electrons can tunnel from one Bi_2Se_3 nanocrystal to another, and if the interface has a substantial number of traps, trap-assisted tunneling contributes to additional conduction, including the following steps: tunneling from electrode to trap, emission from trap to conduction band, which is essentially the Poole-Frenkel emission, and Fowler–Nordheim-like tunneling from trap to conduction band. The Fowler–Nordheim theory governs the FESEM phenomena from semiconductor nanostructures with the emission current associated with the bias voltage in the expression $\ln\left(\frac{I}{V^2}\right) \propto \left(\frac{1}{V}\right)$.[53] The Bi_2Se_3 nanocrystals show nonlinear variation of $\ln\frac{I}{V^2}$ with $1/V$ (Figure 7c), and even though the higher and lower voltage ranges in the figure look linear, the magnified curve near the zero bias is nonlinear, which indicates the absence of cold emission behavior in these nanocrystals, in contrast to the Bi_2Se_3 nanoflakes.[52] The conduction in Bi_2Se_3 nanocrystals was further analyzed for the trap using the Poole–Frenkel theory, which states that $\ln\left(\frac{I}{V}\right) \propto \sqrt{V}$. Interestingly, $\ln(I/V)$ varies linearly with $\sqrt{V}$ for the lower voltage (Figure 7d), suggesting the presence of Poole–Frenkel-type conduction, similar to the case of multilayer Bi_2Se_3 devices.[53] The differential conductance map was generated from this current–voltage characteristic of the Bi_2Se_3 nanocrystals showing a differential conductance minimum near the zero bias (Figure 7e). However, the presence of nonzero differential conductance at the zero bias is consistent with the presence of trap states and can be seen in

DOI: 10.1021/acsanm.9b01941
ACS Appl. Nano Mater. 2020, 3, 274–282

Figure 7d, which dominates over the widely known Dirac cone features[54] in the Bi_2Se_3 nanocrystals.

3. CONCLUSION

The (0001)-oriented hexagon-shaped nanocrystal plates of Bi_2Se_3 were synthesized by the hot-injection method using a nontoxic solvent. The hexagon-shaped morphology with around 40 nm thickness and 600 nm lateral size was achieved because of the supersaturation state. The presence of hexagonal lattice fringes with a lattice spacing of the hexagonal crystal structure in the HRTEM images of these nanocrystals confirms its orientation along [0001]. The Raman spectra of these nanocrystals endorse stabilization of the $R\bar{3}m$ crystallographic group of Bi_2Se_3. The XPS spectra show that the nanocrystals are stable even after exposure to the atmosphere, and the Bi $4d_{5/2}$ and $4d_{3/2}$ peaks show blue shifts of about 4.0 and 3.58 eV, respectively. These nanocrystals show expanded $E_g \sim 0.66$ eV, which is nearly 3 times that of the Bi_2Se_3 single crystals. The first-principles DFT calculations suggest that expanded E_g of these nanocrystals is due to the phenomenal surface band dispersion. The DFT calculations provide evidence of expansion of E_g of the (0001) surface of Bi_2Se_3 from 0.38 to 0.63 eV with an increase of the surface for the same thickness, which demonstrates that the competition between covalent and van der Waals interactions determines the topological state of Bi_2Se_3. The Bi_2Se_3 nanocrystals dispersed between the Ag contact pads exhibit thermally activated behavior with Poole−Frenkel-type conduction because of the electron trapping/detrapping barriers between the Bi_2Se_3 nanocrystals. This manuscript describes the methodologies for fabrication, characterization, and band-structure simulation of Bi_2Se_3. This result will help the scientific community to evaluate the real usefulness and development of device technology.

4. EXPERIMENTAL AND THEORETICAL SECTION

Material Synthesis. The Bi_2Se_3 nanostructures were prepared at different temperatures by a chemical hot-injection method. Commercial-grade Bi_2O_3 (99.999%) and elemental Se (99.99%) powders were chosen as the precursors, while 1-octadecane and oleic acid were used as the solvent and reducing agent, respectively. These chemicals were purchased from Sigma-Aldrich and used without further purification. To prepare the Bi precursor, 1 mmol of Bi_2O_3 was mixed with 5 mL of oleic acid and 20 mL of octadecane in a round-bottom flask. These chemicals were mixed vigorously using a magnetic or mechanical stirrer for 60 min, then heated to 100 °C, and kept at that temperature for 30 min for degassing. After degassing, the mixture was heated to 250 °C for 360 min under a nitrogen flow, and a transparent yellow solution was obtained. The precursor was cooled to 60 °C. In a typical synthesis, the elemental Se powder was mixed in 15 mL of octadecane in another round-bottom flask. The solution was mixed vigorously using a magnetic or mechanical stirrer for 60 min, then heated to 100 °C, and kept at that temperature for 30 min for degassing. Further, the solution temperature was increased to 150 °C (or 200, 250, and 300 °C) and kept at that temperature for 120 min, and then the Bi precursor solution was injected. Then the solution was aged for 60 min at 150 °C (or 200, 250, and 300 °C) under a nitrogen flow. Finally, the solution was cooled to room temperature, washed with ethanol and hexane (1:3 ratio) several times, and centrifuged, and finally the product was dried at 60 °C.

Material Characterization. The phase of these nanoplates was characterized by a Rigaku Smartlab X-ray diffractometer with Cu Kα radiation (λ = 1.5405 Å). The Raman spectra were recorded on a Jobin-Yvon LabRAM HR800UV spectrometer equipped with a highly efficient thermoelectrically cooled charge-coupled device. The spectra were taken at different temperatures in the backscattering configuration using a 632 nm emission line of a He−Ne laser with a laser power 1 μW to 10 mW on the sample surface. The morphological studies were carried out by using FESEM (FEI Quanta Inspect-F) with an accelerating voltage of 30 kV and HRTEM (FEI Tecnai-G^2 T20) with an operating voltage of 200 kV. Chemical analysis of the as-grown Bi_2Se_3 nanostructures was performed by XPS (Specs GmbH, Germany). The spectra were recorded using an Al Kα excitation ($h\nu$ = 1486.6 eV) source, operated at 10 mA and 10 kV. The base vacuum inside the analyzer chamber was 2×10^{-10} Torr and operated in a large-area mode with a pass energy of 30 eV and a step size of 0.1 eV. The UV transmission spectra of the dispersed Bi_2Se_3 nanostructures were recorded using a PerkinElmer LAMBDA 950 UV−vis−near-IR (NIR) spectrophotometer with an assessable wavelength range of 175−3300 nm with a deuterium lamp (UV region) and a tungsten−halogen lamp (vis−NIR region) having a resolution of ≤0.05 nm for the UV−vis region and ≤0.2 nm for the NIR region. The transport measurement was carried out using a setup comprised of an Advanced Research System (ARS) made closed-cycle cryostat, which can be operated from ∼7 to 400 K, a Lakeshore temperature controller, a Keithley picoammeter, and a Keysight nanovoltmeter.

Computational Details. First-principles electronic structure calculations of Bi_2Se_3 were performed through the QE[51] simulation package using a slab model. The hexagonal crystal structure of Bi_2Se_3 was generated through *VESTA*[55] using experimental lattice parameters. The (0001) surface was constructed using *VESTA* and *X-Crysden* software for different thicknesses starting from 1 QL (5 atoms) to 12 QLs (60 atoms). A vacuum layer of 15 Å was used in each slab calculation to avoid interaction with the nearest-neighboring atoms. All calculations were performed within the generalized gradient approximation using the projector-augmented-wave-type scalar relativistic pseudopotential with a Perdew−Burke−Ernzerhof exchange-correlation functional. Band structure calculations were performed both without and with the SOC effects. For SOC calculations, fully relativistic pseudopotentials were used. The plane-wave cutoff was set at 50 Ry units with a charge density cutoff of 200 Ry units for the plane-wave basis set on a $6 \times 6 \times 1$ Monkhorst−Pack k-mesh grid for structure relaxation and a denser k-mesh grid of $8 \times 8 \times 1$ for total energy optimization and band-structure calculations. Each structure undergoes relaxed calculations to obtain the atomic positions near their equilibrium values with a force on each atom of $<10^{-3}$ eV/Å.

AUTHOR INFORMATION

Corresponding Author

*Email: Padhan@iitm.ac.in.

ORCID

Prahallad Padhan: 0000-0002-2020-3812

Notes

The authors declare no competing financial interest.

ACKNOWLEDGMENTS

We thank the SEED faculty grant of IIT Madras for providing the experimental setup and HPCE IIT Madras for the computational facility.

REFERENCES

(1) Qi, X. L.; Zhang, S.-C. Topological Insulators and Superconductors. *Rev. Mod. Phys.* **2011**, *83* (4), 1057−1110.

(2) Zhang, H.; Liu, C.-X.; Qi, X.-L.; Dai, X.; Fang, Z.; Zhang, S.-C. Topological insulators in Bi_2Se_3, Bi_2Te_3 and Sb_2Te_3 with a Single Dirac Cone on the Surface. *Nat. Phys.* **2009**, *5* (6), 438−442.

(3) Analytis, J. G.; McDonald, R. D.; Riggs, S. C.; Chu, J.-H.; Boebinger, G. S.; Fisher, I. R. Two-Dimensional Surface State in the Quantum Limit of a Topological Insulator. *Nat. Phys.* **2010**, *6*, 960−964.

DOI: 10.1021/acsanm.9b01941
ACS Appl. Nano Mater. 2020, 3, 274−282

(4) Kong, D.; Randel, J. C.; Peng, H.; Cha, J. J.; Meister, S.; Lai, K.; Chen, Y.; Shen, Z.-X.; Manoharan, H. C.; Cui, Y. Topological Insulator Nanowires and Nanoribbons. *Nano Lett.* **2010**, *10*, 329−333.
(5) Mntungwa, N.; Rajasekhar, P. V. S. R.; Ramasamy, K.; Revaprasadu, N. A simple route to Bi_2Se_3 and Bi_2Te_3 nanocrystals. *Superlattices Microstruct.* **2014**, *69*, 226−230.
(6) Vargas, A.; Basak, S.; Liu, F.; Wang, B.; Panaitescu, E.; Lin, H.; Markiewicz, R.; Bansil, A.; Kar, S. The Changing Colors of a Quantum Confined Topological Insulator. *ACS Nano* **2014**, *8*, 1222−1230.
(7) Ali, Z.; Cao, C.; Li, J.; Wang, Y.; Cao, T.; Tanveer, M.; Tahir, M.; Idrees, F.; Butt, F. K. Effect of synthesis technique on electrochemical performance of bismuth selenide. *J. Power Sources* **2013**, *229*, 216−222.
(8) Kong, D.; Dang, W.; Cha, J. J.; Li, H.; Meister, S.; Peng, H.; Liu, Z.; Cui, Y. Few-Layer Nanoplates of Bi_2Se_3 and Bi_2Te_3 with Highly Tunable Chemical Potential. *Nano Lett.* **2010**, *10*, 2245−2250.
(9) Zhang, J.; Peng, Z.; Soni, A.; Zhao, Y.; Xiong, Y.; Peng, B.; Wang, J.; Dresselhaus, M. S.; Xiong, Q. Raman Spectroscopy of Few-Quintuple Layer Topological Insulator Bi_2Se_3 Nanoplatelets. *Nano Lett.* **2011**, *11*, 2407−2414.
(10) Yang, X.; Wang, X.; Zhang, Z. Synthesis and optical properties of single-crystalline bismuth selenide nanorods via a convenient route. *J. Cryst. Growth* **2005**, *276*, 566−570.
(11) Peng, H.; Lai, K.; Kong, D.; Meister, S.; Chen, Y.; Qi, X.-L.; Zhang, S.-C.; Shen, Z.-X.; Cui, Yi. Aharonov−Bohm interference in topological insulator nanoribbons. *Nat. Mater.* **2010**, *9*, 225−229.
(12) Ramezani, M.; Sobhani-Nasab, A.; Davoodi, A. Bismuth selenide nanoparticles: simple synthesis, characterization, and its light harvesting applications in the presence of novel precursor. *J. Mater. Sci.: Mater. Electron.* **2015**, *26*, 5440−5445.
(13) Jiang, Y.; Hao, M.; Jiang, L.; Liu, F.; Liu, Y. Shape and Stoichiometry Control of Bismuth Selenide Nanocrystals in Colloidal Synthesis. *RSC Adv.* **2016**, *6*, 47840−47843.
(14) Sun, L.; Lin, Z.; Peng, J.; Weng, J.; Huang, Y.; Luo, Z. Preparation of Few-Layer Bismuth Selenide by Liquid-Phase-Exfoliation and Its Optical Absorption Properties. *Sci. Rep.* **2014**, *4*, 4794.
(15) Ambrosi, A.; Sofer, Z.; Luxa, J.; Pumera, M. Exfoliation of Layered Topological Insulators Bi_2Se_3 and Bi_2Te_3 via Electrochemistry. *ACS Nano* **2016**, *10*, 11442−11448.
(16) Hong, S. S.; Kundhikanjana, W.; Cha, J. J.; Lai, K.; Kong, D.; Meister, S.; Kelly, M. A.; Shen, Z.-X.; Cui, Y. Ultrathin Topological Insulator Bi_2Se_3 Nanoribbons Exfoliated by Atomic Force Microscopy. *Nano Lett.* **2010**, *10*, 3118−3122.
(17) Martinez, G.; Piot, B. A.; Hakl, M.; Potemski, M.; Hor, Y. S.; Materna, A.; Strzelecka, S. G.; Hruban, A.; Caha, O.; Novák, J.; Dubroka, A.; Drašar, Č.; Orlita, M. Determination of the energy band gap of Bi_2Se_3. *Sci. Rep.* **2017**, *7*, 6891.
(18) Nechaev, I. A.; Hatch, R. C.; Bianchi, M.; Guan, D.; Friedrich, C.; Aguilera, I.; Mi, J. L.; Iversen, B. B.; Blugel, S.; Hofmann, P.; Chulkov, E. V. Evidence for a direct band gap in the topological insulator Bi_2Se_3 from theory and experiment. *Phys. Rev. B: Condens. Matter Mater. Phys.* **2013**, *87*, 121111.
(19) Post, K. W.; Chapler, B. C.; He, L.; Kou, X.; Wang, K. L.; Basov, D. N. Thickness-dependent bulk electronic properties in Bi_2Se_3 thin films revealed by infrared spectroscopy. *Phys. Rev. B: Condens. Matter Mater. Phys.* **2013**, *88*, 075121.
(20) Orlita, M.; Piot, B. A.; Martinez, G.; Kumar, N. K. S.; Faugeras, C.; Potemski, M.; Michel, C.; Hankiewicz, E. M.; Brauner, T.; Drašar, Č.; Schreyeck, S.; Grauer, S.; Brunner, K.; Gould, C.; Brüne, C.; Molenkamp, L. W. Magneto-Optics of Massive Dirac Fermions in Bulk Bi_2Se_3. *Phys. Rev. Lett.* **2015**, *114*, 186401.
(21) Yang, S.-D.; Yang, L.; Zheng, Y.-X.; Zhou, W.-J.; Gao, M.-Y.; Wang, S.-Y.; Zhang, R.-J.; Chen, L.-Y. Structure-Dependent Optical Properties of Self-Organized Bi_2Se_3 Nanostructures: From Nanocrystals to Nanoflakes. *ACS Appl. Mater. Interfaces* **2017**, *9*, 29295−29301.
(22) Zhang, Y.; He, K.; Chang, C.-Z.; Song, C.-L.; Wang, L.-L.; Chen, X.; Jia, J.-F.; Fang, Z.; Dai, X.; Shan, W.-Y.; Shen, S.-Q.; Niu, Q.; Qi, X.-L.; Zhang, S.-C.; Ma, X.-C.; Xue, Q.-K. Crossover of the three-dimensional topological insulator Bi_2Se_3 to the two-dimensional limit. *Nat. Phys.* **2010**, *6*, 584−588.
(23) Urazhdin, S.; Bilc, D.; Mahanti, S. D.; Tessmer, S. H.; Kyratsi, T.; Kanatzidis, M. G. Surface effects in layered semiconductors Bi_2Se_3 and Bi_2Te_3. *Phys. Rev. B: Condens. Matter Mater. Phys.* **2004**, *69*, 085313.
(24) Dubroka, A.; Caha, O.; Hroncek, M.; Friš, P.; Orlita, M.; Holý, V.; Steiner, H.; Bauer, G.; Springholz, G.; Humlícek, J. Interband absorption edge in the topological insulators $Bi_2(Te_{1-x}Se_x)_3$. *Phys. Rev. B: Condens. Matter Mater. Phys.* **2017**, *96*, 235202.
(25) Khatun, S.; Pal, A. J. Dirac States of 2D Topological Insulators: Effect of Heterovalent Dopant-Content. *Microsc. Microanal.* **2019**, *25*, 1437.
(26) Kong, D.; Cha, J. J.; Lai, K.; Peng, H.; Analytis, J. G.; Meister, S.; Chen, Y.; Zhang, H.-J.; Fisher, I. R.; Shen, Z.-X.; Cui, Y. Rapid Surface Oxidation as a Source of Surface Degradation Factor for Bi_2Se_3. *ACS Nano* **2011**, *5*, 4698−4703.
(27) Green, A. J.; Dey, S.; An, Y. Q.; O'Brien, B.; O'Mullane, S.; Thiel, B.; Diebold, A. C. Surface oxidation of the topological insulator Bi_2Se_3. *J. Vac. Sci. Technol., A* **2016**, *34* (6), 061403.
(28) Orgiani, P.; Bigi, C.; Das, P. K.; Fujii, J.; Ciancio, R.; Gobaut, B.; Galdi, A.; Sacco, C.; Maritato, L.; Torelli, P.; Panaccione, G.; Vobornik, I.; Rossi, G. Structural and electronic properties of Bi_2Se_3 topological insulator thin films grown by pulsed laser deposition. *Appl. Phys. Lett.* **2017**, *110*, 171601.
(29) Cao, H.; Tian, J.; Miotkowski, I.; Shen, T.; Hu, J.; Qiao, S.; Chen, Y. P. Quantized Hall Effect and Shubnikov−de Haas Oscillations in Highly Doped Bi_2Se_3: Evidence for Layered Transport of Bulk Carriers. *Phys. Rev. Lett.* **2012**, *108*, 216803.
(30) Yan, Y.; Liao, Z.-M.; Zhou, Y.-B.; Wu, H.-C.; Bie, Y.-Q.; Chen, J.-J.; Meng, J.; Wu, X.-S.; Yu, D.-P. Synthesis and Quantum Transport Properties of Bi_2Se_3 Topological Insulator Nanostructures. *Sci. Rep.* **2013**, *3*, 1264.
(31) Busch, M.; Chiatti, O.; Pezzini, S.; Wiedmann, S.; Sánchez-Barriga, J.; Rader, O.; Yashina, L. V.; Fischer, S. F. High-temperature quantum oscillations of the Hall resistance in bulk Bi_2Se_3. *Sci. Rep.* **2018**, *8*, 485.
(32) Kadel, K.; Kumari, L.; Li, W. Z.; Huang, J. Y.; Provencio, P. P. Synthesis and Thermoelectric Properties of Bi_2Se_3 Nanostructures. *Nanoscale Res. Lett.* **2011**, *6*, 57.
(33) Wang, B.-T.; Zhang, P. Phonon spectrum and bonding properties of Bi_2Se_3: Role of strong spin-orbit interaction. *Appl. Phys. Lett.* **2012**, *100*, 082109.
(34) Tse, G.; Yu, D. The first principle study: Electronic and optical properties in Bi_2Se_3. *Computational Condensed Matter* **2015**, *4*, 59−63.
(35) Saeed, Y.; Singh, N.; Schwingenschlogl, U. Thickness and strain effects on the thermoelectric transport in nanostructured Bi_2Se_3. *Appl. Phys. Lett.* **2014**, *104*, 033105.
(36) Luo, X.; Sullivan, M. B.; Quek, S. Y. First-principles investigations of the atomic, electronic, and thermoelectric properties of equilibrium and strained Bi_2Se_3 and Bi_2Te_3 including van der Waals interactions. *Phys. Rev. B: Condens. Matter Mater. Phys.* **2012**, *86*, 184111.
(37) Ramasamy, K.; Malik, M. A.; Revaprasadu, N.; O'Brien, P. Routes to Nanostructured Inorganic Materials with Potential for Solar Energy Applications. *Chem. Mater.* **2013**, *25*, 3551−3569.
(38) Sun, Y.; Cheng, H.; Gao, S.; Liu, Q.; Sun, Z.; Xiao, C.; Wu, C.; Wei, S.; Xie, Y. *J. Am. Chem. Soc.* **2012**, *134*, 20294−20297.
(39) Dang, W.; Peng, H.; Li, H.; Wang, P.; Liu, Z. Epitaxial Heterostructures of Ultrathin Topological Insulator Nanoplate and Graphene. *Nano Lett.* **2010**, *10*, 2870−2876.
(40) Liu, X.; Xu, J.; Fang, Z.; Lin, L.; Qian, Y.; Wang, Y.; Ye, C.; Ma, C.; Zeng, J. One-pot synthesis of Bi_2Se_3 nanostructures with rationally tunable morphologies. *Nano Res.* **2015**, *8*, 3612−3620.
(41) Irfan, B.; Sahoo, S.; Gaur, A. P. S.; Ahmadi, M.; Guinel, M. J.-F.; Katiyar, R. S.; Chatterjee, R. Temperature dependent Raman

DOI: 10.1021/acsanm.9b01941
ACS Appl. Nano Mater. 2020, 3, 274−282

scattering studies of three dimensional topological insulators Bi_2Se_3. *J. Appl. Phys.* **2014**, *115*, 173506.
(42) Kim, Y.; Chen, X.; Wang, Z.; Shi, J.; Miotkowski, I.; Chen, Y. P.; Lima Sharma, P. A.; Sharma, A. L. L.; Hekmaty, M. A.; Jiang, Z.; Smirnov, D. Temperature dependence of Raman-active optical phonons in Bi_2Se_3 and Sb_2Te_3. *Appl. Phys. Lett.* **2012**, *100*, 071907.
(43) Yang, X.; Wang, X.; Zhang, Z. Synthesis and optical properties of single-crystalline bismuth selenide nanorods via a convenient route. *J. Cryst. Growth* **2005**, *276*, 566−570.
(44) Moulder, J. F., Stickle, W. F., Sobol, P. E.′, Bomben, K. D.; *Handbook of X-ray Photoelectron Spectroscopy*; Perkin-Elmer Corp., Physical Electronics Division: Eden Prairie, MN, 1992.
(45) Mishra, S. K.; Satpathy, S.; Jepsen, O. Electronic Structure and Thermoelectric Properties of Bismuth Telluride and Bismuth Selenide. *J. Phys.: Condens. Matter* **1997**, *9*, 461−470.
(46) Indirajith, R.; Rajalakshmi, M.; Gopalakrishnan, R.; Ramamurthi, K. Characterization of bismuth selenide (Bi_2Se_3) thin films obtained by evaporating the hydrothermally synthesised nanoparticles. *Superlattices Microstruct.* **2016**, *91*, 165−172.
(47) Manjulavalli, T. E.; Balasubramanian, T.; Nataraj, D. Structural and optical properties of thermally evaporated Bi_2Se_3 thin film. *Chalcogenide Lett.* **2008**, *5* (11), 297−302.
(48) Jiang, Y.; Zhu, Y.-J.; Cheng, G.-F. Synthesis of Bi_2Se_3 Nanosheets by Microwave Heating Using an Ionic Liquid. *Cryst. Growth Des.* **2006**, *6* (9), 2174−2176.
(49) Ahmed, R.; Xu, Y.; Sales, M. G.; Lin, Q.; McDonnell, S.; Zangari, G. Synthesis and Material Properties of Bi_2Se_3 Nanostructures Deposited by SILAR. *J. Phys. Chem. C* **2018**, *122*, 12052−12060.
(50) Dhar, N.; Syed, N.; Mohiuddin, M.; Jannat, A.; Zavabeti, A.; Zhang, B. Y.; Datta, R. S.; Atkin, P.; Mahmood, N.; Esrafilzadeh, D.; Daeneke, T.; Kalantar-Zadeh, K. Exfoliation Behavior of van der Waals Strings: Case Study of Bi_2S_3. *ACS Appl. Mater. Interfaces* **2018**, *10* (49), 42603−42611.
(51) Giannozzi, P.; Baroni, S.; Bonini, N.; Calandra, M.; Car, R.; Cavazzoni, C.; Ceresoli, D.; Chiarotti, G. L.; Cococcioni, M.; Dabo, I.; Dal Corso, A.; de Gironcoli, S.; Fabris, S.; Fratesi, G.; Gebauer, R.; Gerstmann, U.; Gougoussis, C.; Kokalj, A.; Lazzeri, M.; Martin-Samos, L.; Marzari, N.; Mauri, F.; Mazzarello, R.; Paolini, S.; Pasquarello, A.; Paulatto, L.; Sbraccia, C.; Scandolo, S.; Sclauzero, G.; Seitsonen, A. P.; Smogunov, A.; Umari, P.; Wentzcovitch, M. R. QUANTUM ESPRESSO: A Modular and Open-Source Software Project for Quantum Simulations of Materials. *J. Phys.: Condens. Matter* **2009**, *21*, 395502.
(52) Sze, S. M. *Physics of Semiconductor Devices*; John Wiley & Sons: New York, 1981.
(53) Lampert, M. A.; Mark, P. *Current injection in solids*; Academic Press: New York, 1970.
(54) Hanaguri, T.; Igarashi, K.; Kawamura, M.; Takagi, H.; Sasagawa, T. Momentum-resolved Landau-level spectroscopy of Dirac surface state in Bi_2Se_3. *Phys. Rev. B: Condens. Matter Mater. Phys.* **2010**, *82*, 081305.
(55) Momma, K.; Izumi, F. *VESTA 3* for Three-Dimensional Visualization of Crystal, Volumetric and Morphology Data. *J. Appl. Crystallogr.* **2011**, *44*, 1272−1276.

DOI: 10.1021/acsanm.9b01941
ACS Appl. Nano Mater. 2020, 3, 274−282